The Impact of Strong Cathodic Polarization on Ni|YSZ Microelectrodes

Kreka, Kosova; Hansen, Karin Vels; Mogensen, Mogens Bjerg; Norrman, Kion; Chatzichristodoulou, Christodoulos; Jacobsen, Torben

Published in:
Journal of the Electrochemical Society

Link to article, DOI:
10.1149/2.0141805jes

Publication date:
2018

Document Version
Også kaldet Forlagets PDF

The Impact of Strong Cathodic Polarization on Ni|YSZ Microelectrodes

K. Kreka,[1,z] K. V. Hansen,[1] M. B. Mogensen,[1,*] K. Norrman,[1] C. Chatzichristodoulou,[1] and T. Jacobsen[2,*]

[1]*Department of Energy Conversion and Storage, Technical University of Denmark, DTU Risø Campus, DK-4000 Roskilde, Denmark*
[2]*Department of Chemistry, Technical University of Denmark, DK-2800 Kgs. Lyngby, Denmark*

This work is a study of the impact of short-term strong cathodic polarization in a Ni|YSZ model system using Ni probes as working microelectrodes in a high temperature scanning probe microscope at 650°C in humidified 9% H_2 in N_2. Impedance spectroscopy revealed one to three orders of magnitude decrease in the high frequency resistance and four to five orders of magnitude decrease in the low frequency impedance with polarization from −1.06 V to −3.06 V vs E°(O_2), indicating introduction of electronic conductivity and expansion of the reaction zone around the Ni microelectrode. The effect on the Ni|YSZ interface included formation of electronic conductance, reaction between Ni and YSZ and accumulation of impurities around the Ni|YSZ contact as verified by conductance scans of the polarized area. Cyclic voltammetry was used to compare three systems with different impurity levels and showed that the presence of silicates reduces the current, i.e. lowers the performance of the electrode reaction.
 [DOI: 10.1149/2.0141805jes]

Manuscript submitted December 22, 2017; revised manuscript received March 1, 2018. Published March 15, 2018. This was Paper 2863 presented at the Honolulu, Hawaii, Meeting of the Society, October 2–7, 2016.

Solid oxide fuel/electrolysis cells (SOFC/SOEC, collectively termed SOC) are currently one of the most promising reversible energy conversion and storage technologies. A critical challenge for such devices to become economically viable is their long term durability, and therefore a considerable amount of work has been done on understanding their degradation mechanisms. When using a SOC in electrolysis mode, it is economically beneficial to operate the cell at high current density, because it increases the fuel production rate.

Several long-term studies have been performed on SOEC operating at high current densities.[1–3] They have revealed different degradation mechanisms on the fuel electrode. Tao et al.[4] report silica nanoprecipitates inside Ni grains in SOEC which had been operating at current densities higher than 1.5 A/cm^2. Chen et al.[2] have performed post mortem analysis on cells operated for more than 300 hours at high current density. They observed the formation of ZrO_2 nanoparticles on Ni surfaces in cells which were operated at current densities higher than 1 A/cm^2 at 850°C.[2] The formation of the nanoparticles was strongly correlated to the cell polarization and lowered the electrode performance due to loss of Ni percolation. The degradation mechanism on highly polarized Ni-YSZ electrodes was also discussed by Mogensen et al.,[5] and they observed that part of the Ni particles lose their electrical contact to the electrode. It was noted that the region close to the electrolyte after testing had lower Ni content and higher porosity.

In contrast to the long-term testing of SOEC at high current density, short-term tests with very high current densities[3,4,6] and also reverse current treatment,[7] have shown to improve the performance of the cell. Klotz et al.[2] and Szász et al.[3] observe that a nanostructured interlayer between Ni and YSZ, which improves the performance of the SOFC, was formed after operating a SOEC at a current density of 2 A/cm^2 for 10 s.

When an SOEC is operated at high current densities the Ni-YSZ cathode is strongly polarized and electronic conductivity is increased in the YSZ. Electronic conductivity in YSZ is associated with a partial reduction of zirconia which takes place in two steps. The first occurs at low temperatures where electrons are trapped by impurities (e.g. Fe), resulting in a yellow or gray color, and the second happens at higher temperatures where the electrons are trapped in the oxygen vacancies, resulting in blackening of the zirconia.[8] The reduction of zirconia has been studied extensively and coloration has been observed by several authors.[9–11]

Electrochemical reduction of ZrO_2 in Ni-YSZ systems has been studied by several groups and they find that as the cathodic polarization increases, the ZrO_2 will become reduced resulting in formation of Zr dissolved in Ni and intermetallic Ni-Zr phases.[6,12–15] Thermodynamic calculations show that at 650°C a potential below −2.4 V vs. E(pO_2 = 1 bar) is required for the reduction of ZrO_2 into pure Zr[13,15] whereas solid solution of Zr-Ni and intermetallic phases are formed at lower cathodic polarizations than the ZrO_2 reduction. Thus, YSZ is reduced at higher electrode potentials when in contact with Ni. Additionally, under cathodic polarizations, Ni interacts with silicate impurities. According to the Ni-Si-O phase diagram Si forms intermetallic phases with Ni for pO_2 below 10^{-37} bar.[16] Thus, under cathodic polarizations to potentials below −1.8 V vs. E(pO_2 = 1 bar) silica may be reduced.

SOC electrodes possess a complex microstructure which includes a multicomponent porous structure with various particle sizes. Traditional studies of SOC using current-voltage curves (IV) and electrochemical impedance spectroscopy (EIS), provide invaluable information about the overall performance of the cell, but do not reveal the highly inhomogeneous spatial distribution of the potential losses. At present time we still have a limited understanding of the implications of the spatial heterogeneities of the potential losses in the SOC durability. Therefore, in this study an in situ localized probing approach is implemented to investigate the Ni-YSZ electrode under cathodic polarizations. Electrochemical measurements are carried out using Ni probes with small radii of curvature in contact with polished YSZ surfaces in a Controlled Atmosphere High Temperature Scanning Probe Microscope (CAHT-SPM). The CAHT-SPM offers the opportunity to perform highly localized in situ studies of the Ni|YSZ cathode system due to only applied cathodic polarizations without the influence of microstructure (porosity, particle size, size distribution etc.). The measurements are supplemented with Scanning Electron Microscopy (SEM) and Time of Flight Secondary Ion Mass Spectrometry (ToF-SIMS) performed before and after the electrochemical measurements to reveal microstructural or chemical changes caused by the polarization. As silicate impurities are[17–19] the measurements are carried out on YSZ samples with different concentrations of silica. The high temperature in situ localized probing in synergy with surface chemical and microstructural investigation represents an important advancement in the characterization of the Ni/YSZ electrodes in SOECs.

*Electrochemical Society Fellow.
[z]E-mail: kkre@dtu.dk

Experimental

Nickel probe and sample preparation.—The nickel probes were produced in-house, using 250 μm (99.98% purity, Alfa Aesar) or 100 μm diameter Ni wires (99.994% Ni, Alfa Aesar). The 250 μm wire contains less than 10 ppm of Al, Si, Co, Mg, Co, Cr and Fe and 23 ppm of C. The impurities in the 100 μm thick Ni wire consist of 12 ppm of Fe, 10 ppm of C, 5 ppm of O, 2 ppm of Cr and S, and 1 ppm of Co. The impurity data for both types of wires were provided by the manufacturer. The Ni wires were cut in pieces of 3 cm in length and one end was bent in a *z* shape so that the wire could be handled easily. The sharpening of the tip was done by electrochemical etching of the Ni using 2 M KCl as electrolyte and Pt wire as cathode.[20] The Ni wire itself was the anode. A DC potential of 2.5 to 3 V was applied across the Ni and the Pt wire. After obtaining a sharp tip, the wire was pressed to create a flat surface, which serves as a reflecting surface for the laser beam in the scanning probe microscope (SPM). The end of the tip was then bent so that it formed roughly a 75 degree angle from the cantilever's body. The other 15 degree inclination was offered by the probe holder on which the probe was welded. The tip was thus perpendicular to the surface of the sample. The tip geometry was verified before the experiments using scanning electron microscopy (SEM).

8 mol% yttria-stabilized zirconia (8YSZ) powder (TZ8Y, Tosoh) was pressed uniaxially and isostatically using 87 and 275 MPa pressure, respectively, and then sintered in air at 1550°C for 2 hours. The final pellets were 10 mm in diameter and 1 mm in thickness. They were polished on one side, finishing with 0.1 μm diamond suspension. Additionally, YSZ samples with 1000 ppm of Si were produced following the same procedure. The Si was introduced in the sample by mixing 8YSZ powder with 0.2 wt% SiO_2 (Alfa Aesar) (0.43 mol %). The powder mix was diluted in ethanol to ensure a uniform mixture and was dried while being mixed on a hot plate at 60°C for 24 hours. After sintering and polishing, all the pellets were cleaned using 37% hydrochloric acid in ultrasonic bath for 2 min, then milli-Q water and later ethanol in ultrasonic bath for 5 min each, and finally they were dried using a nitrogen gun.

8 mol% YSZ single crystals were purchased from MTI Corporation with the size 10 × 10 × 1 mm^3. The polished surface had the (100) orientation. A zigzag scratch was applied to the sample using a diamond tip with the purpose of tracking the polarization spots. The crystals were cleaned in ethanol in ultrasonic bath for 5 min and dried using a nitrogen gun.

Experimental set-up.—The electrochemical characterization, the surface conductance and topography measurements were carried out in a controlled atmosphere high temperature scanning probe microscope (CAHT-SPM)[21,22] a diagram of which is shown in Figure 1 .The samples were placed on the heating plate and held down by three alumina pins, which were held in place by steel springs. A platinum wire, used as a macroscopic counter and reference electrode, was attached at the edge of the samples and held in place by one of the alumina pins. The conductance images were acquired in scanning mode, where each pixel of the image represents a single frequency impedance measurement. The AC voltage with a 10 kHz frequency and 0.5 V amplitude was generated by a Stanford RS830 lock-in amplifier and was applied across the Pt counter electrode and the Ni tip. The current response was measured by the lock-in amplifier through a 1 MΩ resistor connected in series with the tip. The resistor protects the lock-in amplifier from any overload.[23] Since these measurements were conducted in contact mode the resolution of the technique was determined by the electrical probe-sample contact area. Surface conductance and topography images were obtained simultaneously.

Additionally, the set-up has the capability of performing electrochemical measurements where the SPM tip is used as a working electrode, and it is pressed against the surface of the sample for the duration of the measurements. Since the Ni tips were fabricated in-house their dimensions vary slightly. On the basis of the force constant calculated from the dimensions of the cantilever,[24] the force applied to the probe

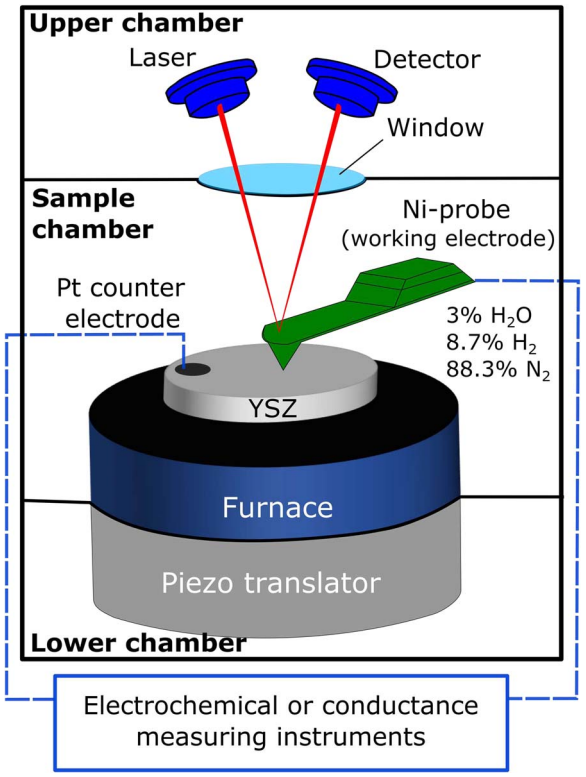

Figure 1. Schematic drawing of the CAHT-SPM. The atmosphere in the sample chamber contains 3% H_2O, 8.7% H_2 and 88.3% N_2 unless noted otherwise.

was estimated to be between 0.2 and 2 μN. However, within each data set the force was kept constant unless noted differently. For the electrochemical measurements, such as electrochemical impedance spectroscopy (EIS), cyclic voltammetry (CV) and chronoamperometry, a Gamry Instruments FAS2 Femtostat was used. The surface temperature of the sample was determined utilizing a thermocouple placed at the surface of the sample in a separate calibration experiment. The temperature of the sample/tip contact was most likely underestimated due to the fact that the thermocouple/sample contact is larger than the sample/tip contact, therefore the cooling effect is more pronounced.

Most measurements were carried out at 650°C in a 9% H_2/N_2 mixture humidified at room temperature by bubbling the gas through water. The electrochemical measurements were carried out using a two-electrode set up. Due to the large size difference between the working electrode (Ni tip-sample micro-contact) and counter electrode (Pt wire-sample macro-contact), the polarization of the counter electrode was negligible. Thus, the counter electrode also acted as reference electrode, and the reference potential was the equilibrium potential of the H_2/H_2O electrode reaction in the atmosphere applied, at the same temperature (650°C). The oxygen partial pressure, pO_2, of the exhaust gas was continuously monitored with a YSZ-based oxygen sensor operating at 1000°C. Once the desired experimental temperature was reached, a waiting time of a minimum 30 min was applied for the temperature and the pO_2 to stabilize. When the pO_2 is stabilized a small decrease in the reference potential of roughly 5–10 mV is observed in a time period of five hours.

For the humidified 9% H_2/N_2 atmosphere, the measured oxygen potential of −940 mV vs. air at 1000°C corresponds to pH_2O/pH_2 ratio of 0.309 at the outlet. In the case where the temperature of the water used to humidify the atmosphere was 25°C and the gas was saturated, an experimental environment of 3% H_2O, 8.7% H_2 and 88.3% N_2 (i.e. a pH_2O/pH_2 ratio of 0.34) was expected. The difference between the measured and the theoretical pH_2O/pH_2 was small and corresponds to a change of less than 5 mV in the reference potential

Table I. Samples types and impedance series acquired for each sample. *i* and *d* refer to increasing and decreasing potentials. F_1 and F_2 refer to two different contact forces applied on the tip.

Type of Sample	Tip/Sample couple	EIS series name
YSZ	A	YSZ-A_i
		YSZ-A_d
	B	YSZ-B F_1
		YSZ-B F_2
	C	YSZ-C
SiYSZ	D	SiYSZ-D_i
		SiYSZ-D_d
	E	SiYSZ- E
YSZ100	F	YSZ100-F_{i-d}
	G	YSZ-G

which is insignificant for the purpose of the experiments. From the pH_2O/pH_2 ratio determined by the pO_2 monitor the reference electrode potential at 650°C was calculated to be −1.066 V vs. $E^\circ(O_2)$. From one experiment to another, variations of the water temperature were observed, which result in a reference potential fluctuation of less than 20 mV. For dry 9% H_2/N_2, the measured oxygen potential of −1035 mV at 1000°C corresponds to a pH_2O/pH_2 of 0.055 at the outlet, which corresponds to a reference potential of −1.135 V vs. $E^\circ(O_2)$ at 650°C.

DC polarizations starting from 0 V down to −2 V versus the reference potential with a step size of −0.1 V or −0.2 V were carried out. The current response, later referred to as chronoamperometry or conditioning period, of each applied polarization was recorded for 120–300 s before recording the EIS response under continued constant DC polarization. EIS measurements were recorded in the frequency range from 82 kHz to 0.082 or 0.0082 Hz using 10 mV rms with 7 points per decade.

A list of the samples used for electrochemical measurements is reported in Table I.

A fresh tip and sample was used for each experiment. The sample-tip couples are indicated by the letters A through G. With YSZ-A, SiYSZ-D and YSZ100-F, two data sets were collected, one with increasing (from −2 V up to 0 V vs. E_{ref}) and one with decreasing (from 0 V down to −2 V vs. E_{ref}) potentials, noted with *i* and *d* subscripts, respectively. With YSZ-B, two series of decreasing potentials (i.e. increasing polarizations) were acquired with two different contact forces, where the F_2 series has a 50% higher force than F_1. Additional experiments with decreasing polarization were performed with probe C, E and G on YSZ, SiYSZ and YSZ100 respectively.

To obtain post-mortem information about the surface chemistry and morphology of the contact region in the YSZ sample time of flight secondary ion mass spectrometry (ToF-SIMS) imaging and SEM were performed. Additionally, the contact surface of the nickel tip was investigated using SEM and energy dispersive X-ray spectroscopy (EDS) (Zeiss Supra or Zeiss Merlin). The ToF-SIMS analysis was performed using a ToF-SIMS IV (ION-TOF GmbH, Munster, Germany). The ion beam used for imaging was a 25 keV Bi^+ pulsed beam, with a 10 kHz frequency and a pulse length of 100 ns. Prior to imaging, a larger area (750 × 750 μm^2) was sputtered using 30 nA of 3 keV Xe^+ for 45 s to remove any hydrocarbon species adsorbed on the surface. The surface was flushed with 20 eV electrons to reduce surface charging.

Results

Electrochemical measurements on Ni|YSZ.—A series of impedance measurements were performed at polarizations stepped from 0 to −2 V and back to 0 V in steps of 0.1 V or 0.2 V and with a conditioning period of 300 s before each spectrum was recorded. Figure 2 shows conditioning currents as a function of time at selected polarizations. The behavior of the current evolves from capacitive to inductive with increasing polarization. In other words, under low cathodic polarization (Figure 2a), the cathodic current decreases with time, like the response of a resistor - capacitor (RC) in parallel, while at high cathodic polarization an increasing cathodic current is observed (Figure 2c), i.e. like that of a parallel resistor-inductor (RL) behavior.

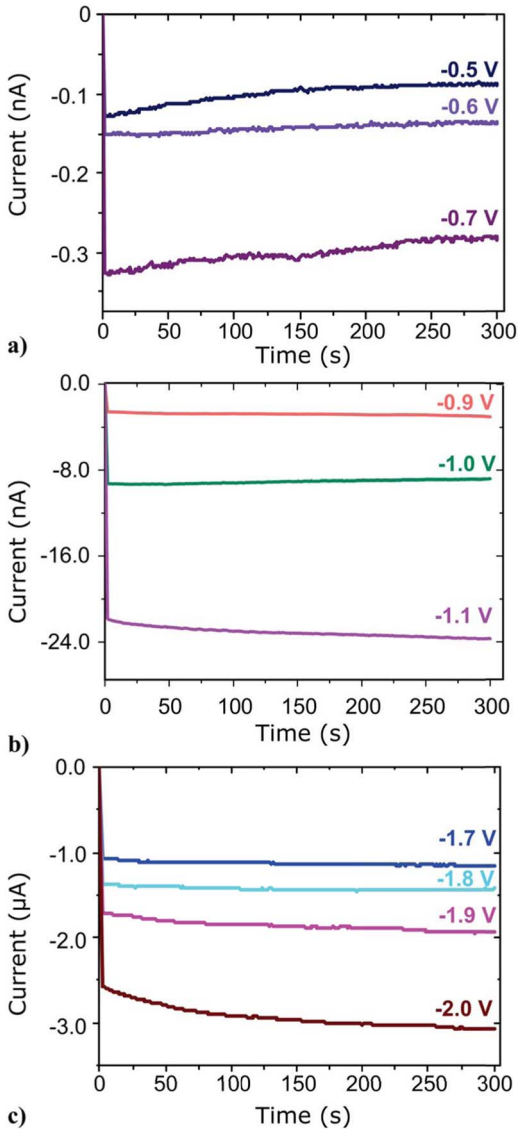

Figure 2. Time dependence of the current during different polarizations at a) low cathodic polarization, b) intermediate polarization and c) high cathodic polarization for the YSZ-A sample. At low cathodic polarization the relaxation shows RC behavior while at high cathodic polarization RL behavior is observed.

Impedance spectra acquired upon increasing cathodic polarizations are shown in Figure 3. The impedance spectra evolve significantly with increasing polarization. From 0 V to −0.8 V, only one suppressed arc is present in the impedance spectra. A new arc becomes visible in the low frequency regime at −0.9 V. Furthermore, at low frequency an inductive loop is present at polarizations between −1.1 V and −1.5 V. Other series of impedance measurements with frequencies as low as 0.0082 Hz, reveal inductive loops from −1 V to −2 V, as illustrated in Figure 4.

As the results obtained with frequency range from 82 kHz to 0.082 Hz did not allow a reasonable extrapolation of the inductive loops to DC, the width of the spectra was used as a describing parameter instead of the DC polarization resistance. It is referred to as the intercept resistance ($R_{x\text{-}L}$) and is determined as the distance from the high frequency extrapolation (R_s) to the low frequency intersection of

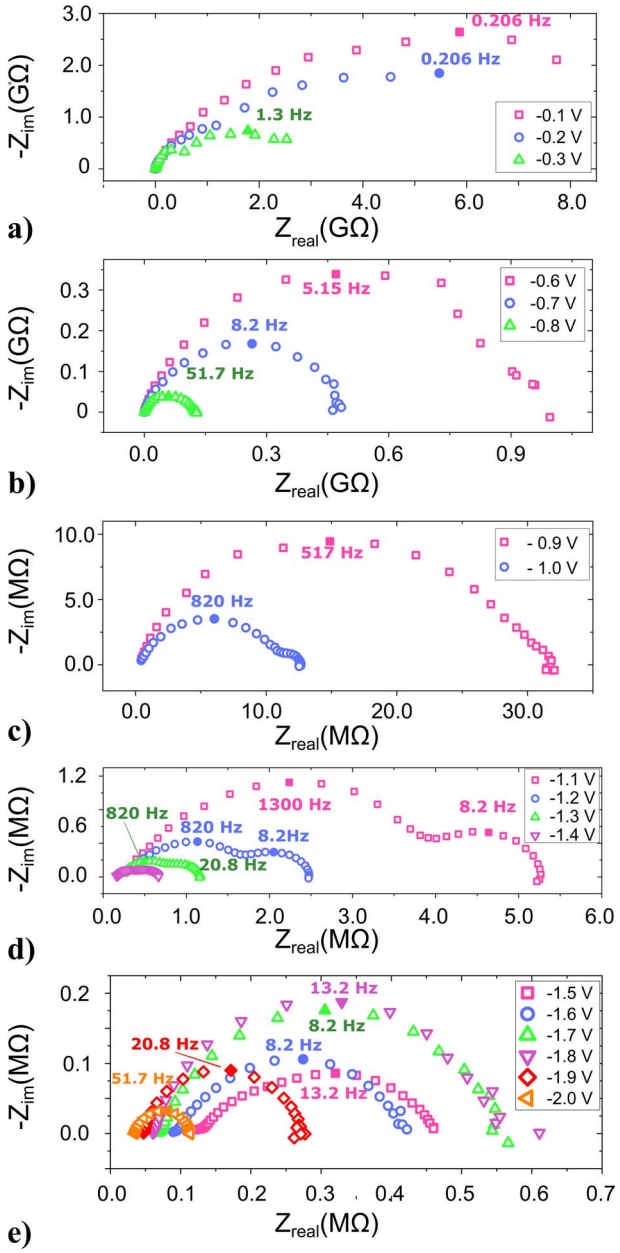

Figure 3. a-e) EIS spectra recorded for Ni|YSZ (YSZ-A) under varying DC polarization at 650°C in humidified 9% H_2/N_2. The lowest frequency is 0.082 Hz. Summit frequencies and polarizations are given in the figure.

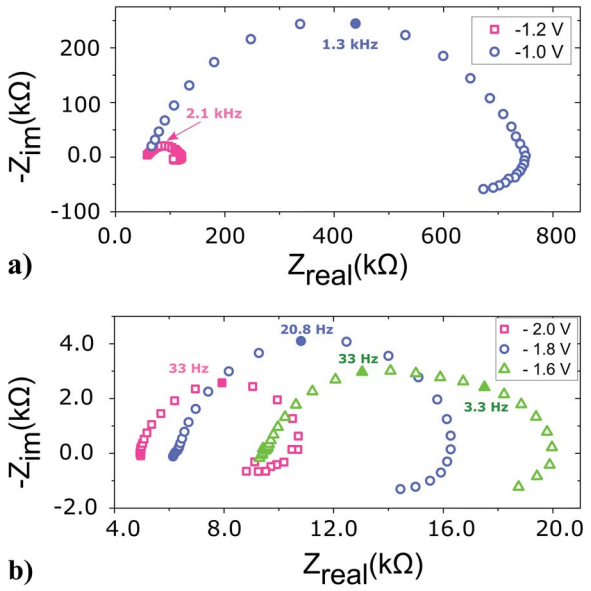

Figure 4. Impedance spectra obtained in the frequency range from 82 kHz to 0.0082 Hz showing inductive loops at low frequencies. These spectra are taken form YSZ-B F_2 series.

the real axis. In the $R_{x\text{-}L}$ notation, x-L stands for real axis intercept at low frequency. Figure 5 shows the R_s and $R_{x\text{-}L}$ of several different polarization series. The R_s and $R_{x\text{-}L}$ values corresponding to the impedance spectra shown in Figure 3 are shown in Figures 5a and 5b respectively (YSZ-A_d). The R_s values were obtained by fitting an equivalent circuit with R_s in series with a RQ parallel combination to the high frequency data, whereas the $R_{x\text{-}L}$ values were read from the graphs. When determining R_s by fitting was not possible, the R_s values were read from the graphs. While the cathodic polarization increases from 0 V to −1 V, R_s stays constant. For cathodic polarizations stronger than −1 V, R_s decreases. This decrease varies from a factor of two to almost two orders of magnitude from one polarization series to another as shown in Figure 5. The intercept resistance, $R_{x\text{-}L}$, shows a more consistent behavior across different data series than R_s. Almost one order of magnitude decrease of the $R_{x\text{-}L}$ is observed upon increasing polarization down to −0.7 V. A steeper decrease of roughly three orders of magnitude of the $R_{x\text{-}L}$ follows for polarizations down to −1.4 V. For polarizations between −1.4 V and −1.7 V the $R_{x\text{-}L}$ displays an increase followed by a decrease down to −2 V. For an overall increase of the cathodic polarization of two volts, $R_{x\text{-}L}$ decreases by 4–5 orders of magnitude.

The R_s and $R_{x\text{-}L}$ for the decreasing cathodic polarization series are also shown in Figure 5 (YSZ A_i) and they show a similar behavior. It was not possible to extract values of the $R_{x\text{-}L}$ between −0.3 V and 0 V because the summit frequency was too far below the frequency range used for the measurements to obtain a valid extrapolation. However, the extracted $R_{x\text{-}L}$ points follow the same trend as for the increasing cathodic polarization. The R_s during the increasing cathodic polarization deviates from the decreasing cathodic polarization, especially at low cathodic polarizations.

Electrochemical measurements on Ni|SiYSZ.—A similar study was performed for the Ni|SiYSZ interphase, and Figure 6 shows a series of impedance spectra obtained upon increasing cathodic polarization. The chronoamperometry measurements during the conditioning time show similar behavior as that for Ni|YSZ shown in Figure 2. Similar to the Ni|YSZ system, the impedance spectra show the presence of one arc from 0 V to −0.9 V. At −1 V a clear emergence of a second arc is observed at low frequencies. Contrary to the Ni|YSZ impedance spectra, the two arcs are clearly separated in the Ni|SiYSZ system. As the low frequency arc becomes more prominent, the two arcs do not merge but remain very well separated. Additionally, the beginning of the low frequency arc shows a straight line behavior (∼45 degree slope) at −1.1 and −1.2 V. The inductive behavior in the Ni|SiYSZ sample is only observed from −1.8 V to −2 V for frequencies down to 0.1 Hz. The inductive loops may be visible at lower cathodic polarizations if lower frequencies are probed.

The values of the high frequency resistance (R_s) and intercept resistance ($R_{x\text{-}L}$) for several series are obtained in the same manner as for the Ni|YSZ system and are shown in Figures 7a and 7b, respectively. In addition to the R_s and $R_{x\text{-}L}$ extracted from the series shown in Figure 6 (SiYSZ-E) an additional series with 0.2 V step in both increasing (SiYSZ-D_d) and decreasing (SiYSZ-D_i) cathodic polarizations is shown in Figure 7. The $R_{x\text{-}L}$ and R_s of the Ni|YSZ and the Ni|SiYSZ system show generally similar behaviors with some minor differences. The R_s vs. potential curve of Ni|SiYSZ does not show a plateau at low cathodic polarization, and a steeper decrease

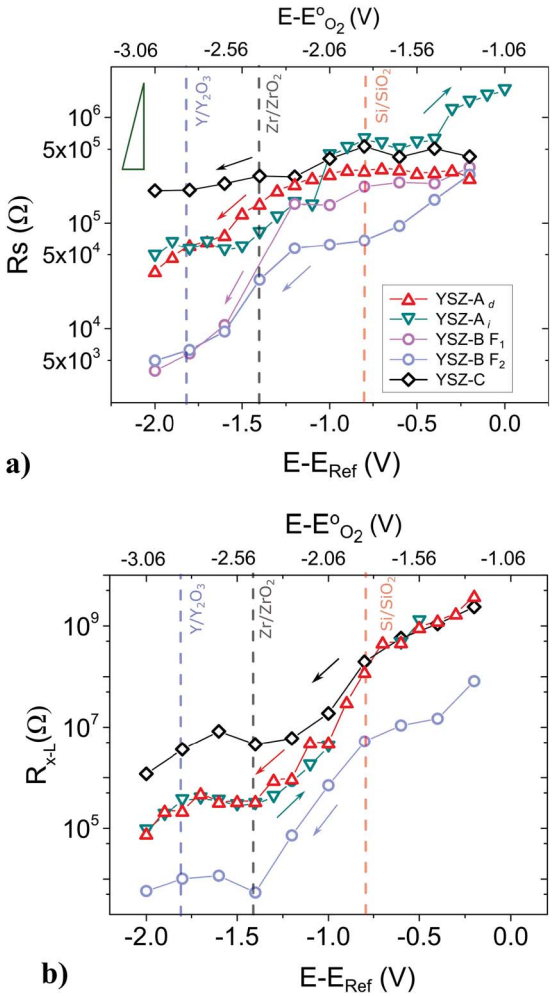

Figure 5. a) The semi-log plot of R_s and b) $R_{x\text{-}L}$ of Ni|YSZ as a function of the applied potential versus the reference potential (bottom x-axis). The A, B and C indicate the tip used for the series. The corresponding potential versus oxygen is shown in the top x-axis. The Si/SiO_2, Zr/ZrO_2 and Y/Y_2O_3 equilibrium potentials are indicated with red, black and blue dashed lines, respectively. The green triangle in a) indicates the equilibrium relation between potential and R_s when electronic conductivity is introduced in YSZ.

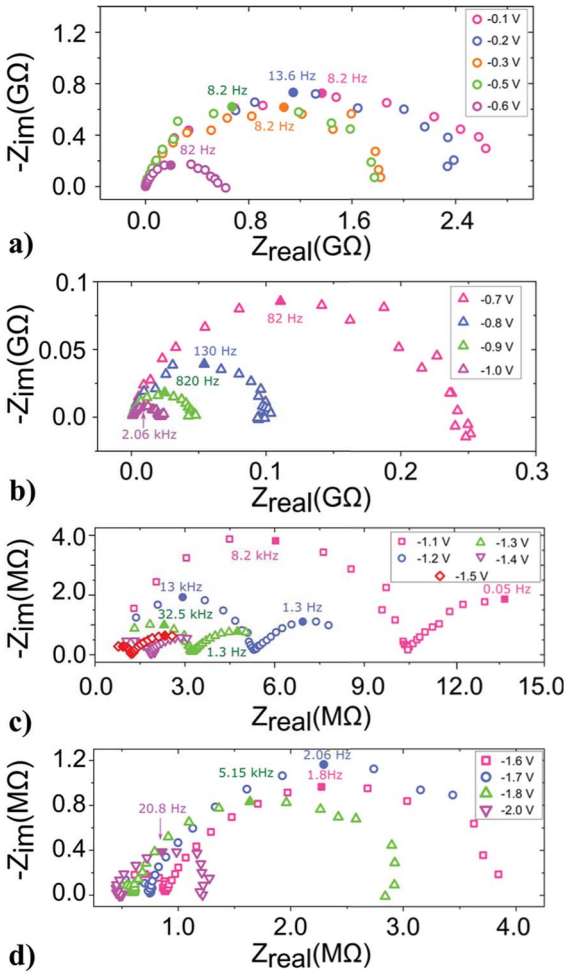

Figure 6. a)-d) Impedance spectra of Ni|SiYSZ (SiYSZ-D_i) at different polarization voltages. Frequency range: 82 kHz – 0.082 Hz. This data set was performed using a very sharp tip (sub-micron diameter).

is observed at cathodic polarizations stronger than −1.6 V. The $R_{x\text{-}L}$ activation behavior of the Ni|SiYSZ shows three different activations, a slow decrease of $R_{x\text{-}L}$ at low polarizations (0 V down to −0.5 V), followed by a steeper decrease at intermediate (−0.6 V down to −1.4 V) and at high polarization (−1.6 V down to −2 V), where the last two sections are separated by a small increase or a plateau (−1.4 V down to −1.6 V). The $R_{x\text{-}L}$ decreases by four to five orders of magnitude for both systems.

Electrochemical measurements on Ni|YSZ100.—Impedance spectra obtained with single crystal YSZ electrolyte show similar behavior to the previous two systems. The R_s and $R_{x\text{-}L}$ of two different series are shown in Figures 8a and 8b, respectively. The YSZ100-D series shows the R_s and $R_{x\text{-}L}$ in both increasing (−0.1 V steps) and decreasing (0.2 V steps) cathodic polarizations. The R_s show an overall decrease of approximately one order of magnitude in the increasing cathodic polarization series, where the steepest decrease is observed from −1.4 V down to −1.8 V. The R_s values at low cathodic polarizations do not return to the same value when the electrode potential is increased. At −0.6 V, the R_s is a factor of two smaller in the decreasing series compared to the same electrode potential in the increasing series. In the decreasing direction the series finishes at −0.4 V due to loss of contact between the tip and the sample. The second series shows an increase in the R_s at low cathodic polarizations, followed by a small decrease from −0.8 V to −1.4 V. The steepest decrease is observed from −1.4 V to −1.8 V.

The $R_{x\text{-}L}$ for both series show very similar behavior, where an overall 4–5 orders of magnitude decrease is observed. A small decrease was observed from 0 V to −0.7 V followed by a steep decrease down to −1.6 V. Finally, the $R_{x\text{-}L}$ increases by approximately a factor of two from −1.6 V to −2 V. When increasing the electrode potential, $R_{x\text{-}L}$ remains suppressed and up to two orders of magnitude difference is observed compared to the starting value.

Cyclic voltammetry.—Figure 9a shows voltammograms recorded for the three systems. In Figure 9b they are shown normalized to their highest cathodic current for better comparison. The voltammograms follow similar trends in all the studied systems, namely in all the CVs inductive hysteresis is observed.

With increasing cathodic polarization in the Ni|YSZ100 system a strong increase in the cathodic current starts at −1.4 V. This increase starts at lower polarizations (−1.2 V) for the Ni|YSZ while the Ni|SiYSZ system shows a more gradual increase that starts at −0.6 V to −0.8 V followed by a steeper increase down to −1.6 V. CVs for both Ni|YSZ and Ni|SiYSZ have an inflection point at −1.4 V. Indications of an inflection point in Ni|YSZ100 are observed between −1.6 and −1.8 V. In Figure 9c the inverse $R_{x\text{-}L}$ values and the first derivative of the current with respect to polarization are compared to better illustrate this behavior. All data are individually normalized

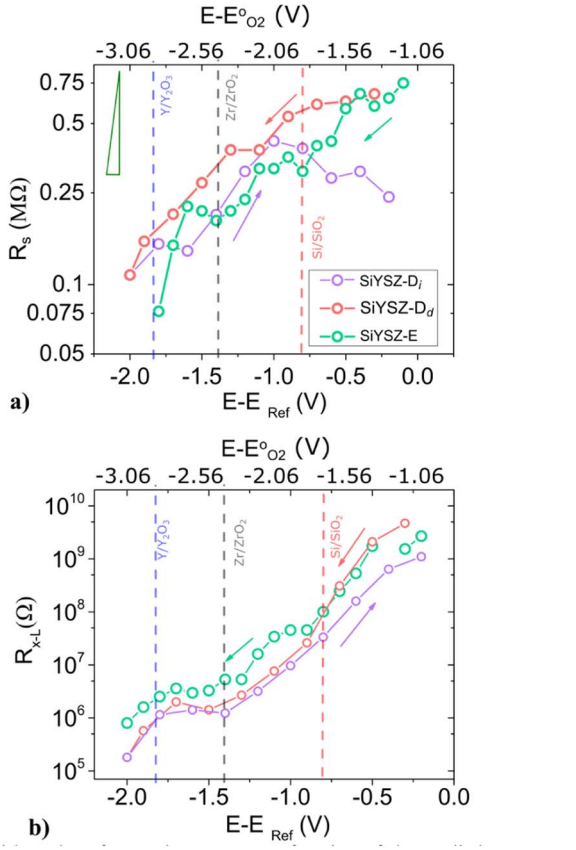

Figure 7. a) The Ni|SiYSZ semi-log plot of R_s and b) $R_{x\text{-}L}$ as a function of the applied potential versus the reference potential (bottom x-axis). The corresponding potential versus oxygen is shown in the top x-axis. The Si/SiO_2, Zr/ZrO_2 and Y/Y_2O_3 equilibrium potentials are indicated with red, black and blue dashed lines respectively. The green triangle in a) indicates the equilibrium relation between potential and Rs when electronic conductivity is introduced in the YSZ.

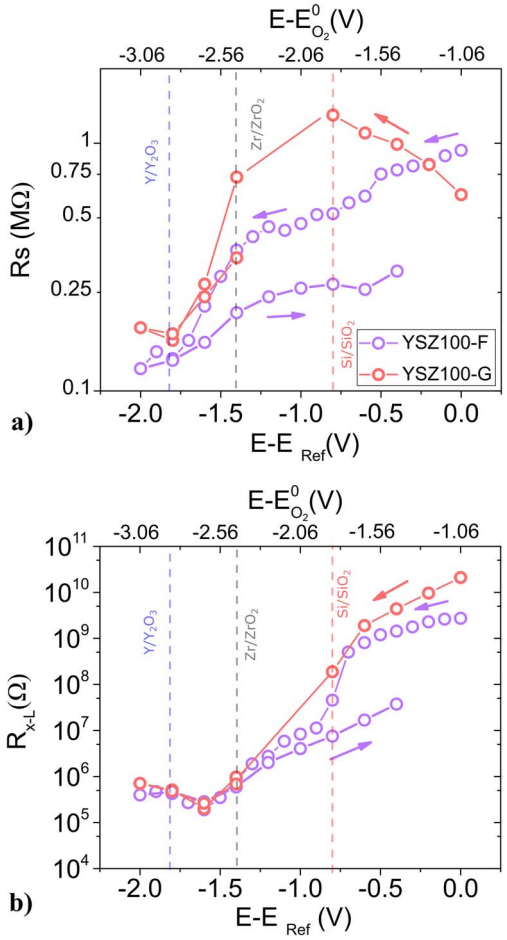

Figure 8. a) The Ni|YSZ100 semi-log plot of R_s and b) $R_{x\text{-}L}$ as a function of the applied potential versus the reference potential (bottom x-axis) both in the increasing and decreasing cathodic polarization (purple). A second series is also included (red). The corresponding potential versus oxygen is shown in the top x-axis. The Si/SiO_2, Zr/ZrO_2 and Y/Y_2O_3 equilibrium potentials are indicated with red, black and blue dashed lines, respectively.

to their highest numerical value. The $R_{x\text{-}L}$ values are calculated from the impedance spectra obtained after polarizations of 300 s, while the CVs are obtained with a sweep rate of 10 mV/s.

The difference observed between the current values at high cathodic polarizations could be due to the different contact areas. The contact radii are calculated using the Newman formula:[26]

$$R_s = \frac{1}{4\sigma r} \qquad [1]$$

where R_s is the high frequency resistance, σ is the bulk conductivity of YSZ in air and r is the radius of the contact. This formula is valid for a circular contact area, a homogeneous electrolyte conductivity and negligible contact resistance contribution to the serial resistance, i.e. R_s originates solely from the electrolyte resistance. Thus, using this formula for this system is a crude approximation. The radii are given together with the normalization factors in Figure 9b. The current densities at −2 V (currents used to perform the normalization) are normalized to the tip circumference and to the tip area using the estimated Newman radius and shown in Table II. The normalized current densities increase with sample purity.

The water partial pressure during the measurements has a substantial impact on the cathodic current, as shown in Figure 9d. The voltammograms were acquired using the same sample and the same tip during the same day, but at two different positions on the sample. The general behavior is quite similar but in the wet 9% H_2/N_2 (pH_2O/pH_2 of 0.306) the cathodic current at −2 V is almost twice the value of the current in the dry 9% H_2/N_2 (pH_2O/pH_2 of 0.055).

Conductance mapping.—Figure 10 shows a conductance map of a polarization spot on a single crystal YSZ100-G obtained at 650°C after applying a polarization of −2 V versus the reference for 40 min. The image is somewhat blurry due to the bold tip after prolonged contact at a large contact force. However, a low conductance region and a high conductance region can be observed. The difference in conductance between them is more than one order of magnitude.

Chemical and microstructural investigation of the Ni|YSZ contact region.—For additional chemical analysis, ToF-SIMS was performed on a YSZ sample polarized from 0 V to −2 V with −0.2 V step size. Conductance scanning was avoided to exclude any artifacts on the ToF-SIMS images due to possible spreading of impurities[23] while scanning in contact mode, since the ToF-SIMS is extremely sensitive to surface contamination. A large surface area of the YSZ was mapped by ToF-SIMS, and the Ni signal was used as indicator of the Ni|YSZ contact area. Figure 11a through f show ToF-SIMS ion images of the contact area between the Ni probe and YSZ. In addition to the Zr, Y and Ni maps, Si, Na and Ca maps are shown. A lateral distribution of Ni is shown in both Figure 11a, which indicates the shape and size of the contact area. Si is enriched in a roughly circular area with a diameter of 50 μm around the contact area, i.e. approximately four times the diameter of the Ni tip. A SEM image of the Ni-tip used in this experiment is shown in Figure 11h and reveals a contact area with approx. 12 μm in diameter. Figure 11g shows a SEM image of

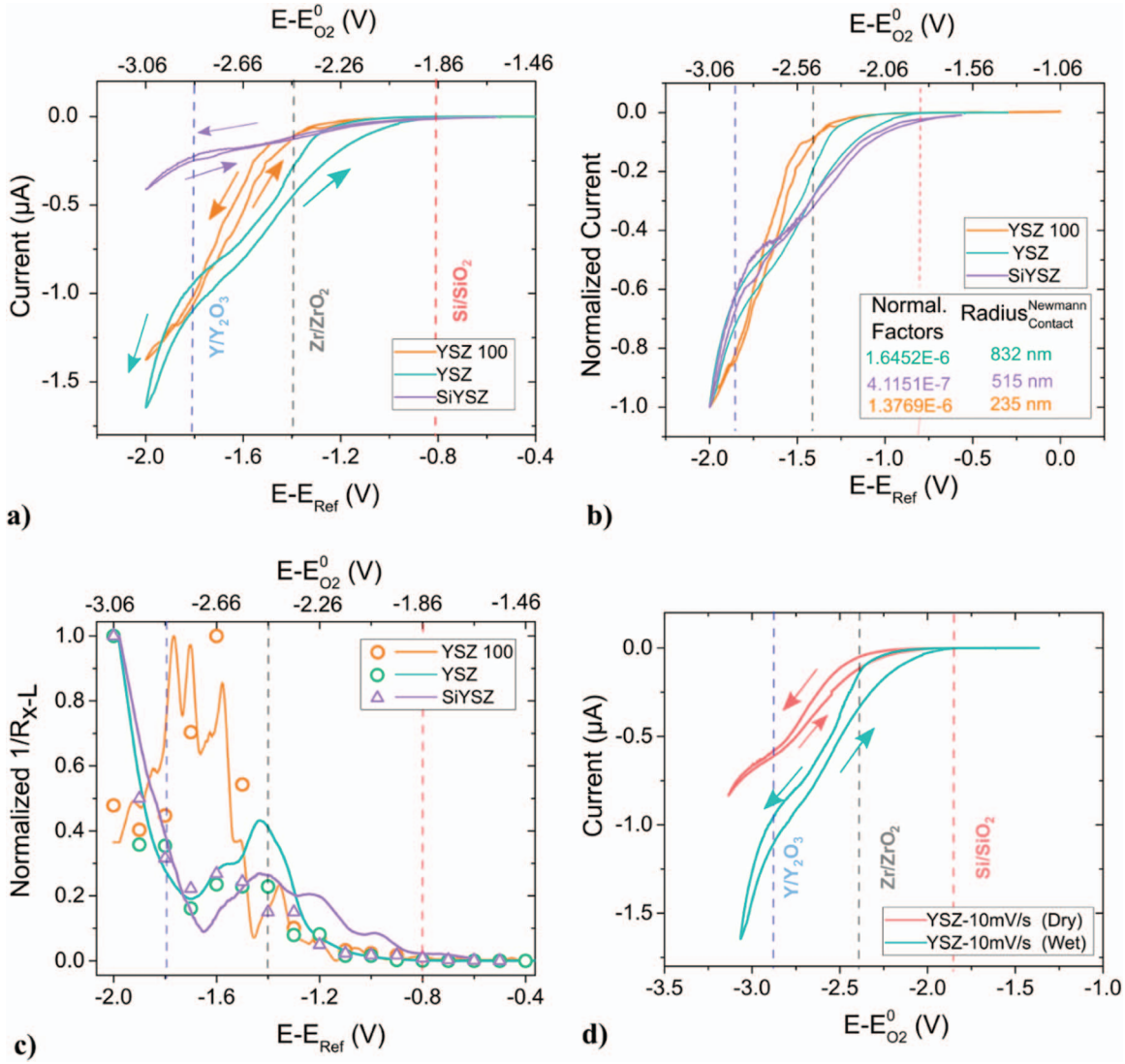

Figure 9. a) Cyclic voltammetry for Ni|SiYSZ (purple), Ni|YSZ (blue) and Ni|YSZ100 (orange) in humidified 9% H_2/N_2 at 650°C. The sweep rate for all CV is 10 mV/s. b) CV curves normalized to the highest cathodic current. c) The first derivative of the CV for all systems (in continuous line) and the inverse $R_{x\text{-}L}$ obtained from impedance measurements. d) Cyclic voltammetry in the Ni|YSZ system in dry and wet 9% H_2/N_2. The reference potential in dry 9% H_2/N_2: −1.135 V, in wet: −1.066 V. The corresponding water partial pressures are: 0.055 and 0.306 for the dry and wet respectively.

the contact area on YSZ. From this SEM image it is obvious that the surface of the YSZ contacted by the Ni tip is substantially roughened. Despite the presence of Ni and Si, both Y and Zr are also observed in the region. Further investigations, such as SEM and EDS of the tips used for the strong polarizations revealed the presence of Si and Al oxide species in the contact region as well as on the walls of the tip.

Discussion

The chronoamperometry measurements at different potentials on the Ni|YSZ system, as shown in Figure 2, indicate that the current evolves from capacitive to inductive with increasing polarization. This behavior is further supported by the appearance of inductive loops at low frequencies in the impedance spectra seen in Figures 3 and 4. Inductive loops have been previously observed in metal|YSZ systems,[26–28] and they have been attributed to either the potential dependency of the concentration of adsorbed intermediate species[29–31] or to the increase of the reaction zone[32] by the injection of electrons in the YSZ.

At low cathodic polarizations, the water splitting reaction does not extend far from the tip. Due to the high electrode overpotential and concentration of electrons close to the electrolyte/tip contact, we suggest that the reaction rate in the region close to the Ni|YSZ contact is limited by the steam diffusion rate. This region is indicated with

Table II. Estimated radii of the contact points using Eq. 1 with R_s at 0 V. The line and area current densities at −2 V were calculated using the estimated radii.

Sample	Estimated radius (nm)	Current at - 2 V (A)	Line current density (A/cm)	Area current density (A/cm^2)
YSZ 100	235	$-1.38 \cdot 10^{-6}$	$-9.35 \cdot 10^{-3}$	−795
YSZ	832	$-1.65 \cdot 10^{-6}$	$-3.16 \cdot 10^{-3}$	−76
SiYSZ	515	$-4.11 \cdot 10^{-7}$	$-1.27 \cdot 10^{-3}$	−49

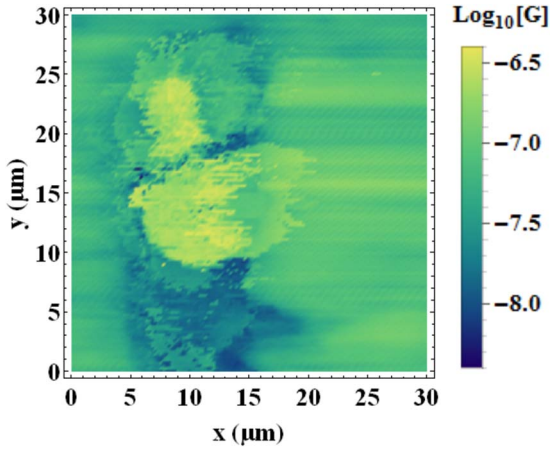

Figure 10. Conductance map of a polarization spot recorded at 650°C after applying a polarization of −2 V vs. E_{ref} for 40 min.

a continuous black line in Figure 12. As the cathodic polarization is increased, the reaction zone extends further away from the tip due to introduction of electronic conductivity in the YSZ. This is represented with the dashed line at the gas|YSZ interface in Figure 12. When an AC signal is superimposed on the steady state polarization, a damped electron concentration wave is created as indicated by the red line in Figure 12. At high frequencies, this concentration wave does not extend beyond the steam diffusion-limited area (shown in Figure 12). Therefore, the high frequency process in the EIS is attributed to the charge transfer reaction at the tip|YSZ interface while the low frequency arc, which appears at higher cathodic polarizations, is attributed to the YSZ|gas surface reaction. The impedance measurements for both Ni|YSZ and Ni|SiYSZ shown in Figure 3, Figure 4 and Figure 6 consistently show a splitting of one arc into two arcs at potentials below −0.8 V and −1. 0 V reflecting two serial processes as explained above. YSZ100 exhibits a similar behavior.

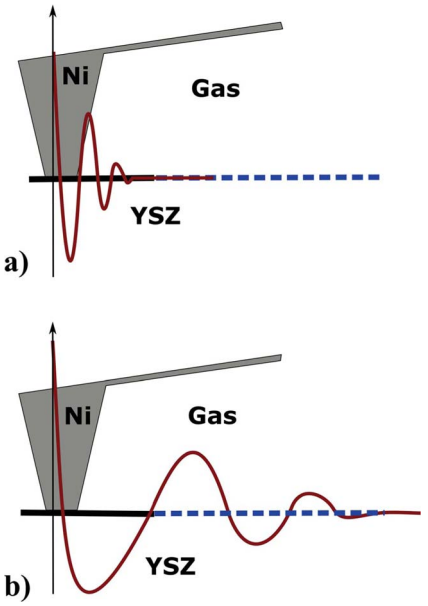

Figure 12. Schematic of the electron concentration (red line) close to the Ni|YSZ contact when an AC signal is applied a) the high frequency case and b) the low frequency case. The gas|YSZ interface is represented using continues line for the surface where the water diffusion is limiting the surface reaction rate and by a dashed line for the surface where there is no water diffusion limitation. Note that the electron concentration variation is only illustrative and is drawn out of scale.

At very low frequencies, the electron concentration wave extends outside of the diffusion limited region, and thus a modulation on the reaction zone is observed. Such modulation causes an inductive loop at low frequencies as seen in Figure 4.

In the series shown in Figure 4 (YSZ-B F_2), however, there is no splitting of the capacitive arcs. The estimated contact radius for the

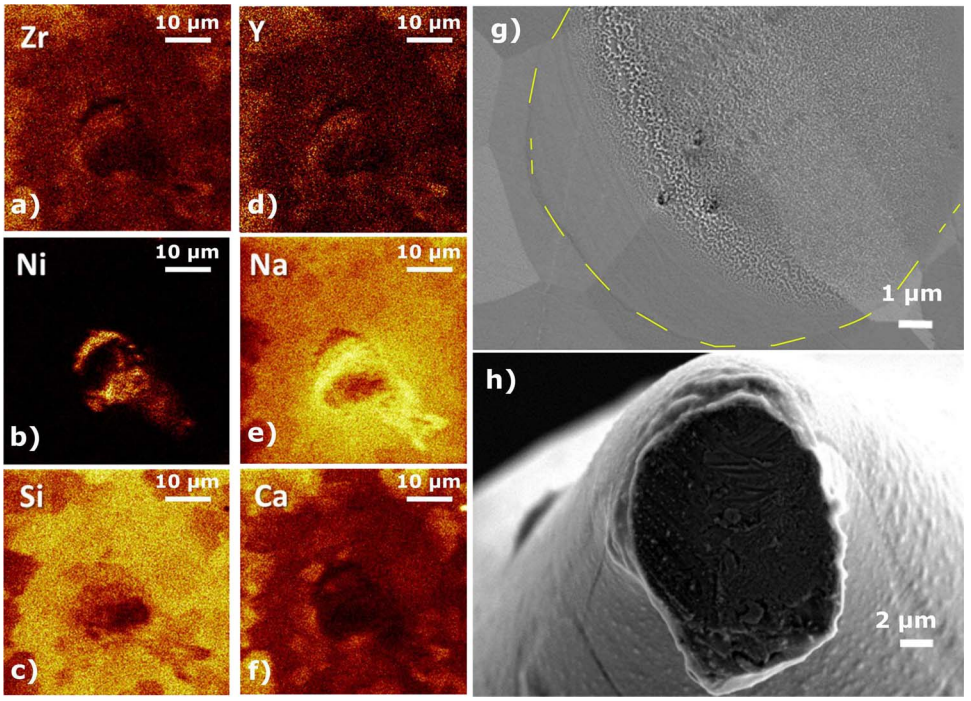

Figure 11. a)-f) ToF-SIMS images (50 × 50 µm^2) of the Ni|YSZ contact area g) SEM image of the YSZ at the contact where the dashed line indicates the border of the modified region and h) SEM image of the Ni tip after the polarization measurement.

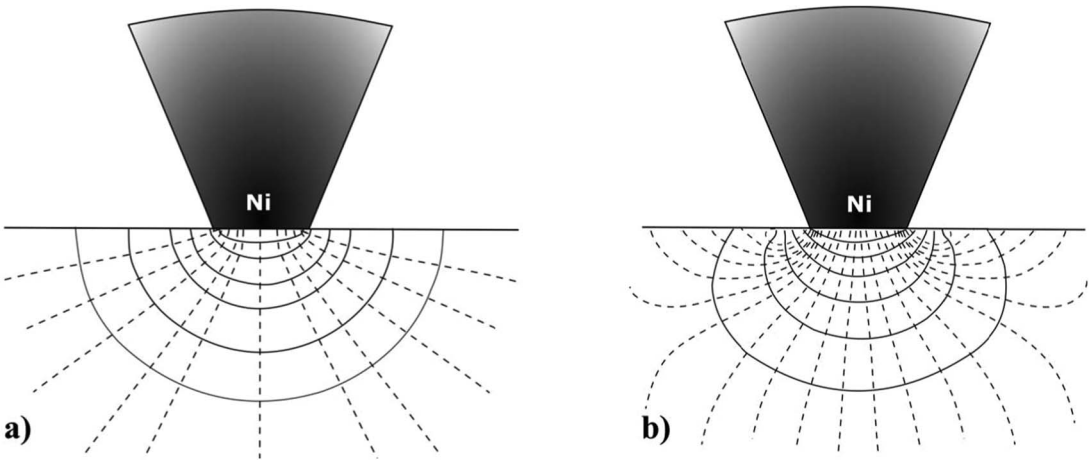

Figure 13. Qualitative sketch of the electron flux (in dashed lines) and the equipotential lines (continuous lines) near the point contact between YSZ and Ni where a) no surface reaction is present b) surface reaction is present.

YSZ-B F_2 is 5 times larger than the contact radius for the YSZ-A_d. Therefore, the details from the YSZ|gas interface impedance may br overshadowed by a relative increase of the parallel Ni|YSZ admittance.

Figure 5, Figure 7 and Figure 8a show that the behavior of R_s is semi-quantitatively similar for the three systems. At low cathodic polarizations (lower than −0.8 V) the uncertainty on the R_s values can be up to 30%. The standard deviation of the R_s from the fits in the low polarization region varies from 20% to 30%, even when only the high frequency region is fitted. For the spectra where the uncertainty was higher than 30% the intercept was estimated from the graphs, instead of fitting the EIS. Due to the large spreading of the impedance spectra of more than 2 orders of magnitude, the uncertainty of the R_s obtained from the estimation of the intercept is also estimated to be 30%. It should be noted that in this region with high frequency impedances in the MΩ range, the values obtained are likely to be influenced by stray capacitances. The stray capacitance of the system was measured to be 0.6 pF, which would give rise to a shunting resistance of 2.65 MΩ at 100 kHz. Therefore, absolute values should be interpreted with care, whereas changes of the R_s with polarization are significant. The extrapolations at higher polarizations are more accurate (< 5% uncertainty at −2 V polarization), except for the SiYSZ samples where the uncertainty obtained from the fit was 15% at −2 V.

The ionic conductivity of YSZ, which can be deduced from the R_s at low cathodic polarizations, is here assumed to be independent of the oxygen partial pressure, while the electronic conductivity depends on the local Fermi potential of the YSZ.[33] When a cathodic polarization lower than −1 V vs. E_{Ref} is applied, the R_s, which is inversely proportional to the conductivity of YSZ, decreases slowly, corresponding to a region where the ionic conductivity is dominant. The cathodic polarization is equivalent to a change in the oxygen partial pressure at the Ni|YSZ interface, and as it increases, an exponential decrease of the R_s (or increase in conductivity) is observed, indicating that the electronic conductivity becomes dominating.

Interpolating from the data of Appel et al.,[34] the ionic conductivity of 8 mol% YSZ at 650°C is 9.7×10^{-3} S cm^{-1}. Using Eq. 1, the high frequency resistance (R_s) at low polarizations and the ionic conductivity, the contact radius is estimated to be 0.8 μm for the series YSZ-A_i in Figure 5. SEM images of the tip show that the geometric radius of the contact area is approximately 7 μm. The discrepancy on the measured versus calculated contact radius is not surprising because, in addition to the irregular and changing shape of the contact area due to modification of the tip during the experiment, the uncertainty of the R_s at low cathodic polarization is the largest. Additionally, SEM images give the final physical contact after the experiment was performed, and the physical area does not necessarily indicate an electrical contact. Therefore, both estimates of the contact area have large uncertainties, and only a semi-quantitative description of the experimental results is possible.

For low pO_2, in equilibrium conditions, the electronic conductivity of YSZ has a $p_{O_2}^{-1/4}$ dependency as reported by Park and Blumenthal.[35] The linear behavior with a slope of −1/4 of the log pO_2 vs. log σ corresponds to a linear behavior in the log R_s versus applied potential with a slope of

$$\frac{\partial \log(R_s)}{\partial E} = \left(2.3026\frac{RT}{F}\right)^{-1} = 5.4$$

where R is the gas constant, T is the sample temperature in Kelvin and F is the Faraday constant. This derivation of the slope assumes that the YSZ conductivity is constant throughout the sample, and that it is purely electronic. Additionally it does not take into account any changes in the electronic conductivity due to the change of the oxide vacancy concentration or the change in the area of the active zone around the tip when the potential is changed. The obtained slopes are 2 to 6 times lower than the equilibrium slope. Thus, as expected the above mentioned assumptions do not hold for our system under polarization. A factor that contributes to the flattening of the R_s vs. applied potential is attributed to the decrease of the electronic conductivity away from the Ni|YSZ interface as a result of the potential distribution in a point contact configuration, as shown in Figure 13a. Additionally, due to the water splitting reaction, the electron concentration near the YSZ surface close to the contact is reduced, thus causing the current lines to loop up to the surface[36] (Figure 13b). This lowers the volume in which electronic conductivity is introduced in the YSZ, hence causing a decrease of the slope of the R_s versus potential. The current and the equipotential lines in Figure 13b are qualitatively drawn but similar behavior was simulated by Ciucci et al.[37] In the case of ceria $(CeO_2)_{0.95}(Y_2O_3)_{0.05}$, studies of the variation of conductivity at different temperatures as a function of pO_2 have shown that its conductivity flattens out at very low polarizations, which shows that the proportionality of the conductivity of ceria with $p_{O_2}^{-1/4}$ breaks for very low pO_2.[38] As the oxygen vacancy concentration is expected to increase upon reduction of YSZ the slope is expected to decrease similar to the case of ceria.[39] Since we use potentials well below the reduction of ZrO_2, partial or full reduction of YSZ is expected; therefore the above relation is not expected to be valid for the entire polarization range.

The $R_{x\text{-}L}$ for all three systems shows similar behavior. For the YSZ100 and YSZ there is a low activation region from 0 V to −0.7 V followed by a steeper activation at stronger polarizations. For the SiYSZ system the second more pronounced activation region starts at −0.5 V. Additionally, all three systems show a tendency to have a local maximum in $R_{x\text{-}L}$ at high cathodic polarizations (−1.6 V for the

SiYSZ and the YSZ and −1.8 V for the YSZ100). The shift in this local maximum toward more negative potentials for the single crystal indicates that the reaction responsible for the increase in the $R_{x\text{-}L}$ is delayed by the slower reducibility of the single crystal in comparison to the polycrystalline samples.

The R_s and $R_{x\text{-}L}$ for the decreasing cathodic polarization series performed in the same spot, immediately after the increasing polarization series to ensure that the probe|YSZ contact conditions were not changed, are shown in Figure 5, Figure 6 and Figure 8. For the Ni|YSZ100 (Figure 8) and the Ni|SiYSZ system (Figure 6), the R_s and the $R_{x\text{-}L}$ do not return to the initial high values indicating a permanent or at least a slowly decaying modification of the YSZ close to the probe contact. For the YSZ system the coincidence of the $R_{x\text{-}L}$ between the anodic and cathodic direction does not suggest any irreversible changes. Notice that the biggest hysteresis is observed in the YSZ100 case, which indicates that the re-oxidation process proceeds slower for the single crystal. Luerssen et al.[10] have observed that it is more difficult to induce electronic conductivity in single crystal YSZ than in polycrystalline samples, which is in line with our findings. This is attributed to the morphology and higher defect density in the polycrystalline sample in comparison to the single crystal.[10] However, previous studies have also shown the fully reversible character of the reduction-oxidation in single crystal YSZ,[40] therefore we attribute the hysteresis in the R_s and $R_{x\text{-}L}$ to the slow re-oxidation rather than to permanent conductivity changes of the YSZ. We explain the slower reoxidation rate of bulk YSZ by the fast "passivation" of the surface region when this is re-oxidized. The oxidized YSZ surface will impede the electronic conduction necessary to oxidize the reduced bulk YSZ below the surface region. Further, the polycrystalline YSZ will have higher electronic conductivity due to impurities concentrated in the grain boundaries and therefore reoxidize faster than the single crystal YSZ.

The CV measurements for all systems (Figure 9) show inductive hysteresis, and their current densities decrease in absolute value with increasing silica content. This behavior indicates that the quantity of silica in the YSZ impedes the H_2O splitting reaction and limits the current. For the SiYSZ and YSZ systems, two different activation regions are observed in the CVs, separated by a flattening of the current at intermediate polarizations. For the single crystal however, only one activation region is observed close to −1.4 V, which coincides with the reduction potential of ZrO_2.

The cathodic current increase at polarizations between −0.6 V and −1.2 V is attributed to the reduction of silicates as it fits with the reduction potential of SiO_2 (−0.8 V) and it is not observed in the single crystal system. For the Ni|SiYSZ system a gradual cathodic current increase starts at lower polarizations than in the Ni|YSZ and Ni|YSZ100, and the flattening/inflection point is most pronounced in the system that contains the most silica and weakest in the purest system, indicating that there is a substantial contribution to the current from the reduction of the silicates in the intermediate polarization region. The second activation region is attributed to the partial reduction of zirconia and the expansion of the reaction zone due to the introduction of electronic conductivity in the reduced region.

The normalized first derivatives of current with respect to polarization and the normalized inverse $R_{x\text{-}L}$ are in good agreement for all the studied systems as shown Figure 9c. The discrepancies observed are partly due to the fact that the time it takes to acquire the CV data is much shorter than the impedance series where the polarization is stepped down by 0.1 V or 0.2 V. Inflection points in the CV curves are indicated as local maxima and local minima in the derivative curves and clearly these inflection points shift toward higher polarizations for the single crystal, suggesting once more that the lack of grain boundaries delays its reduction.

The doubling of the cathodic current with a 6-fold increase of the steam partial pressure that is seen at −2 V in Figure 9d is related to the spreading of the contact area at strong polarizations, as the CVs were obtained with the same probe, and geometric effects can be excluded. The reaction zone at such polarization spreads beyond the steam diffusion-limited region due to the introduction of electronic conductivity in the YSZ. If the active area around the Ni|YSZ interface is the same at the same pO_2 for both wet and dry atmospheres, the current increase should be the same as the increase in the water partial pressure. However, in the wet environment, due to the higher concentration of steam, more electrons are consumed at the gas|YSZ interface, resulting in a smaller effective reaction zone.

Correlation between surface chemistry, electrochemistry and electrical measurements.—The formation of both high and low conducting regions in the vicinity of the Ni|YSZ contact point as a result of the strong cathodic polarization, as shown by the conductance map in Figure 10, is in accordance with the R_s and $R_{x\text{-}L}$ not returning to their initial high values. Both the R_s behavior and the conductance maps are similar to what was found in the Pt|YSZ system.[36] The low conducting regions are probably due to accumulation of SiO_2, as this is observed by both EDS and ToF-SIMS to be associated with the contact region on the YSZ and on the Ni tip. This is also similar to the Pt-YSZ system.[36] SiO_2 originating from the impurities in the raw materials is normally found to segregate to YSZ surfaces at elevated temperatures and form an impurity film with other present impurities.[41–43] Conductance images of the YSZ before polarization show a uniform conductance. This, however, does not explain the low conductance areas or the proximity to the contact, since a film would have caused a lower conductance through the sample and not localized close to the polarization spot.

The accumulation of the Si-based impurities close to the Ni|YSZ contact as well as the creeping of the impurities up the surface of the Ni tip, may be explained by the Marangoni effect,[44] if it is assumed that the silicates are in a liquid/glassy phase at the testing conditions. The fluid motion is driven by gradients of the surface tension as a result of temperature gradients (thermo-capillary convection) or concentration gradients. When the nickel tip comes in contact with the thin layer of glassy silicates on the surface of the YSZ, the impurities form a concave meniscus due to the surface tension of the glassy phase. The temperature gradient of the YSZ surface and the tip itself causes a surface tension gradient in the impurity layer, where the highest surface tension is observed at the lowest temperature. The motion of the fluid will be toward the highest surface tension, i.e. toward the lowest temperature. Hence, the silicates would accumulate closer to the tip causing the low conductance region. We have observed that the SEM/EDX images of the tip after being held in contact with a SiYSZ sample without applying any polarization indicate that silica impurities creep up the tip, which support the impact of the Marangoni effect. However, investigations of strong cathodic polarizations on a SiYSZ sample using a bend Ni wire placed inside a furnace where the temperature gradients are negligible indicate that there are regions close to or within the contact region which contain higher concentration of silica impurities supporting the idea that the applied potentials modify the impurity films. Thus the accumulation of the silica impurities close to the NiYSZ contact is most likely caused by the combined effect of the polarization as well as the cooling of the probe.

The electrode applied potentials are well below the reduction potential for SiO_2. Additionally thermodynamic calculations predict the Si from the SiO_2 to diffuse into the Ni, as well as the formation of Si-Ni intermetallic.[10] At a later stage, when the electrode potential is high enough the Si will be re-oxidized to SiO_2 as found by Tao et al.[4] This oxidation might occur when the polarization is released. The presence of silica is observed both in the EDX analysis of the Ni-tips and the YSZ samples. The dissolution of metallic Si in Ni may be locally "purifying" the contact between Ni and YSZ. This is further supported by the ToF-SIMS images (Figure 11) where there is a region in the middle of the Ni contact area, which is depleted of Si and Ni but rich in Zr and Y.

The applied potentials are also below the zirconia reduction potential. Additionally, thermodynamic calculations have shown that the stability of ZrO_2 decreases when in contact with Ni,[13] thus allowing the reduction of ZrO_2 and the formation of intermetallic Ni-Zr to occur at higher pO_2 than expected for pure ZrO_2, suggesting that we reduce the zirconia as well. The roughening of the Ni|YSZ contact area, also

observed at higher temperatures in macroscopic system,[12] as shown in SEM images of the YSZ sample, suggests interaction between the Ni probe and the zirconia sample.

Conclusions

The in situ highly localized study of the Ni|YSZ microelectrode system under strong cathodic polarization presented in this work reveals several important features related to the electrochemical reduction of YSZ as well as to the degradation mechanism of the Ni|YSZ cathode system in SOECs. Strong cathodic polarizations using Ni microelectrodes result in substantial changes in the electrical, microstructural and chemical properties of the YSZ. EIS measurements indicate two rate determining processes where the low frequency process, associated with the reduction of H_2O at the gas|YSZ interface (and oscillation of this reaction zone) becomes more dominant at stronger cathodic polarizations. The high frequency process is associated with the charge transfer reaction at the Ni|YSZ contact. One to three orders of magnitude decrease is observed in the high frequency resistance upon increasing cathodic polarization form 0 V to −2 V, indicating introduction of electronic conductivity in all the YSZ samples, which is supported by the presence of high conductance regions in the conductance scans. Additionally, a 4–5 orders of magnitude decrease in the $R_{x\text{-}L}$ suggests increase of the reaction zone from the triple phase boundary to the YSZ surface. The expansion of the reaction zone can be beneficial for the operation of the SOECs, since it yields higher gas conversion rates. The polarization however, also caused roughening of the contact surface due to the interaction of the Ni with the YSZ. Additionally, impurities are accumulated around the Ni|YSZ contact suggesting that the impurity film is modified upon polarization resulting in a non-uniform distribution of impurities. These results increase our understanding of the degradation mechanism of the Ni electrodes where impurity segregation at the Ni|YSZ interface causes blocking of the triple phase boundaries and reduces the reaction rate. The comparison between polycrystalline YSZ, and SiYSZ and single crystal YSZ samples suggests that the reduction and re-oxidation of the single crystal is retarded pinpointing the importance of the grain boundaries in the redox chemistry of YSZ.

Acknowledgment

We acknowledge financial support from ECoProbe (DFF-4005-00129) funded by the Danish Independent Research Council.

ORCID

K. Kreka https://orcid.org/0000-0002-7864-2148
M. B. Mogensen https://orcid.org/0000-0002-0902-0580

References

1. A. Hauch, S. D. Ebbesen, S. H. Jensen, and M. Mogensen, *J. Electrochem. Soc.*, **155**, B1184 (2008).
2. M. Chen, Y. L. Liu, J. J. Bentzen, W. Zhang, X. Sun, A. Hauch, Y. Tao, J. R. Bowen, and P. V. Hendriksen, *J. Electrochem. Soc.*, **160**, 883 (2013).
3. R. Knibbe, M. L. Traulsen, A. Hauch, S. D. Ebbesen, and M. Mogensen, *J. Electrochem. Soc.*, **157**, B1209 (2010).
4. Y. Tao, J. Shao, and S. Cheng, *ACS Appl. Mater. Interfaces*, **8**, 17023 (2016).
5. M. B. Mogensen, A. Hauch, X. Sun, M. Chen, Y. Tao, S. D. Ebbesen, K. V. Hansen, and P. V. Hendriksen, *Fuel Cells*, **17**, 434 (2017).
6. D. Klotz, B. Butz, A. Leonide, J. Hayd, D. Gerthsen, and E. Ivers-Tiffée, *J. Electrochem. Soc.*, **158**, B587 (2011).
7. C. Graves, S. D. Ebbesen, S. H. Jensen, S. B. Simonsen, and M. B. Mogensen, *Nat. Mater.*, **14**, 239 (2014).
8. R. Ben-Michael and D. S. Tannhauser, *Appl. Phys. A*, **53**, 185 (1991).
9. R. E. W. Casselton, *J. Appl. Electrochem.*, **4**, 25 (1974).
10. B. Luerßen, J. Janek, S. Günther, M. Kiskinova, and R. Imbihl, *Phys. Chem. Chem. Phys.*, **316**, 2673 (2002).
11. J. Janek and C. Korte, *Solid State Ionics*, **116**, 181 (1999).
12. K. V. Hansen, M. Chen, T. Jacobsen, K. Thyden, S. B. Simonesen, S. Koch, and M. B. Mogensen, *J. Electrochem. Soc.*, **163**, F1217 (2016).
13. M. Chen, Y. L. Liu, J. J. Bentzen, W. Zhang, X. Sun, A. Hauch, Y. Tao, J. R. Bowen, and P. V. Hendriksen, *J. Electrochem. Soc.*, **160**, F883 (2013).
14. T. Wagner and G. Duscher, *J. Mater. Res.*, **14**, 3340 (1999).
15. T. Wagner, R. Kirchheim, and M. Ruhle, *Acta Metall. Mater.*, **40**, S85 (1992).
16. C. Chatzichristodoulou, M. Chen, P. V. Hendriksen, T. Jacobsen, and M. B. Mogensen, *Electrochim. Acta*, **189**, 265 (2016).
17. Y. L. Liu, S. Primdahl, and M. Mogensen, *Solid State Ionics*, **161**, 1 (2003).
18. T. Horita, H. Kishimoto, K. Yamaji, M. E. Brito, Y. Xiong, H. Yokokawa, Y. Hori, and I. Miyachi, *J. Power Sources*, **193**, 194 (2009).
19. Y. L. Liu and C. Jiao, *Solid State Ionics*, **176**, 435 (2005).
20. M. Cavallini and F. Biscarini, *Rev. Sci. Instrum.*, **71**, 4457 (2000).
21. K. V. Hansen, T. Jacobsen, A.-M. Nørgaard, N. Ohmer, and M. B. Mogensen, *Electrochem. Solid-State Lett.*, **12**, B144 (2009).
22. K. V. Hansen, Y. Wu, T. Jacobsen, M. B. Mogensen, and L. Theil Kuhn, *Rev. Sci. Instrum.*, **84**, 73701 (2013).
23. K. V. Hansen, K. Norrman, and T. Jacobsen, *Ultramicroscopy*, **170**, 69 (2016).
24. M. A. Poggi, A. W. Mcfarland, J. S. Colton, and L. A. Bottomley, *Anal. Chem.*, **77**, 1192 (2005).
25. J. Newman, *J. Electrochem. Soc.*, **113**, 501 (1966).
26. R. J. Aaberg, R. Tunold, M. Mogensen, R. W. Berg, and R. Ødegård, *J. Electrochem. Soc.*, **145**, 2244 (1998).
27. G. Ø. Lauvstad, R. Tunold, and S. Sunde, *J. Electrochem. Soc.*, **149**, E497 (2002).
28. G. Ø. Lauvstad, R. Tunold, and S. Sunde, *J. Electrochem. Soc.*, **149**, E506 (2002).
29. L. Bai and B. E. Conwai, *J. Electrochm. Soc.*, **138**, 2897 (1991).
30. L. Bai and B. E. Conway, *Electrochim. Acta*, **38**, 1803 (1993).
31. B. A. Van Hassel, B. A. Boukamp, and A. J. Burggraaf, *Solid State Ionics*, **48**, 155 (1991).
32. E. J. L. Schouler and M. Kleitz, *J. Electrochem. Soc.*, **134**, 1045 (1987).
33. T. Jacobsen, C. Chatzichristodoulou, and M. B. Mogensen, *ECS Trans.*, **61**, 203 (2014).
34. C. C. Appel, N. Bonanos, A. Horsewell, and S. Linderoth, *J. Mater. Sci.*, **36**, 4493 (2001).
35. J. Park and R. N. Blumenthal, *J. Electrochem. Soc.*, **136**, 2867 (1989).
36. K. V. Hansen, K. Kreka, and T. Jacobsen, *To be published* (2018).
37. F. Ciucci, W. C. Chueh, D. G. Goodwin, and S. M. Haile, *Phys. Chem. Chem. Phys*, **13**, 2121 (2011).
38. H. L. Tuller and A. S. Nowick, *J. Electrochem. Soc.*, **122**, 255 (1975).
39. H. L. Tuller and A. S. Nowick, *J. Phys. Chem. Solids*, **38**, 859 (1977).
40. C. Bonola, P. Camagni, P. Chiodelli, and G. Samoggia, *Radiat. Eff. Defects Solids*, **119–121**, 457 (1991).
41. K. V. Hansen, K. Norrman, and M. B. Mogensen, *Surf. Interface Anal.*, **38**, 911 (2006).
42. A. E. Hughes and S. Badwal, *Solid State Ionics*, **46**, 265 (1991).
43. A. E. Hughes, *J. Am. Ceram. Soc.*, **78**, 369 (1995).
44. F. Brochard, *Langmuir*, **5**, 431 (1989).